FULL ARTICLE

Photoacoustic microscopy for evaluating a lipopolysaccharide-induced inflammation model in mice

Zhendong Guo[1] | Zhe Li[2] | Yuxiao Deng[2]* | Sung-Liang Chen[1,3]*

[1]University of Michigan-Shanghai Jiao Tong University Joint Institute, Shanghai Jiao Tong University, Shanghai, China

[2]Department of Critical Care Medicine, Renji Hospital, School of Medicine, Shanghai Jiao Tong University, Shanghai, China

[3]State Key Laboratory of Advanced Optical Communication Systems and Networks, Shanghai Jiao Tong University, Shanghai, China

*Correspondence
Yuxiao Deng, Department of Critical Care Medicine, Renji Hospital, School of Medicine, Shanghai Jiao Tong University, 160 Pu Jian Road, Shanghai 200127, China.
Email: dengyxlong@hotmail.com
Sung-Liang Chen, University of Michigan-Shanghai Jiao Tong University Joint Institute, Shanghai Jiao Tong University, Shanghai 200240, China.
Email: sungliang.chen@sjtu.edu.cn

Photoacoustic microscopy (PAM) is a noninvasive imaging technique and is excellent to study structural and functional changes in the microcirculation. In this work, a lipopolysaccharide (LPS)-induced inflammation model in mice is noninvasively evaluated by PAM. PAM is used to image the microvascular structural changes in mice for 8 hours after the LPS with different concentrations is applied. Quantitative analysis of five vessel parameters is conducted, which shows that the rate of reduction in microvasculature is highly dependent on the applied LPS concentrations. For low-concentration LPS, changes in the microvasculature are not obvious over the observation period, whereas for high-concentration LPS, quick and marked reduction in the microvasculature is observed. In addition, changes in capillaries are more significant than those in relatively large vessels. The results show that PAM is able to evaluate the inflammation mouse model by studying structural (and potentially functional) changes in the microcirculation. Furthermore, PAM may have potential for early intervention and treatment plan optimization of sepsis by monitoring the microcirculation and inflammatory response.

KEYWORDS

inflammatory response, microcirculation, photoacoustic imaging, photoacoustic microscopy, sepsis
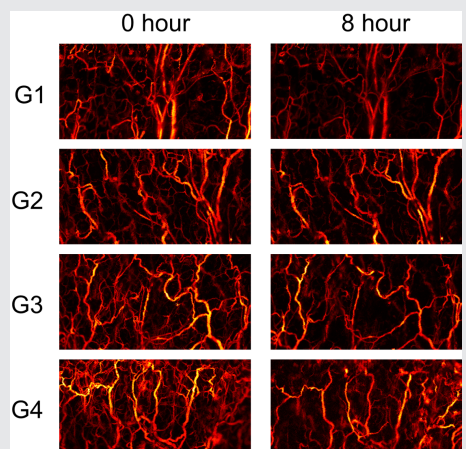
1 | INTRODUCTION

According to the definitions of Sepsis-3, sepsis is defined as life-threatening organ dysfunction caused by a dysregulated host inflammatory response to infection [1]. Sepsis is the primary cause of mortality in critically ill patients. Sepsis and septic shock are lethal with a high mortality rate. The institution of new therapies for sepsis has led to significant reductions in mortality rates [2].

Microcirculation ensures adequate tissue oxygenation and thus organ function. Inflammatory response causes impaired microcirculatory perfusion, which correlates with systemic hemodynamic and oxygen transport indices. Anatomically, there is a significant decrease in capillaries [3]. Functionally, the abnormality is characterized by a decrease in the proportion of capillaries with continuous blood flow,

Zhendong Guo and Zhe Li contributed equally to this work.

in contrast to intermittent or no flow. On the other hand, microcirculatory dysfunction can lead to respiratory distress in tissue cells, which expedites the severity of poor microcirculatory function and leads to organ dysfunction. In this regard, monitoring microcirculatory function is expected to help assess the severity of inflammatory response and thus the treatment of sepsis.

Imaging techniques have been demonstrated to study microcirculation. Videomicroscopy, such as orthogonal polarization spectral (OPS) imaging, provides plentiful information, including vessel morphology, blood flow velocity and heterogeneity of perfusion. OPS imaging technique, however, suffers from the drawback of pressure artifacts due to contact measurements [4]. Laser speckle imaging (LSI) was used to image the distribution of blood flow [5] and can also provide microvascular perfusion maps and assess perfusion heterogeneities [6]. LSI has the disadvantage of vulnerability to motion artifacts. Optical coherence tomography (OCT), a three-dimensional (3D) high-resolution imaging technique, has demonstrated *in vivo* microcirculation imaging of the skin and even capillary reperfusion after ischemic stroke [7, 8]. However, none of the above techniques have the direct capability to access to the blood oxygenation, one of the key functional indices of microcirculatory dysfunction.

To break the limitations of the above imaging tools used in microcirculation and to better assess the severity of inflammatory response, in this work, we explore the feasibility of studying microcirculation in a lipopolysaccharide (LPS)-induced inflammation mouse model (see Supporting Information, Appendix S1 for details) using photoacoustic microscopy (PAM). PAM is a noninvasive, label-free and high-resolution imaging technique [9]. It has high sensitivity to optical absorption and can be used to provide high-quality 3D images of microcirculation. PAM is capable of anatomical, functional and molecular imaging of microcirculation by utilizing a variety of endogenous or exogenous chromophores [10]. Because of the excellent optical absorption contrast of hemoglobin, PAM is particularly useful to acquire vessel morphology and hemodynamic parameters such as oxygen saturation (sO_2), blood flow and metabolic rate of oxygen [11–16]. Specifically, in this study, structural changes in the microcirculation in an LPS-induced inflammation mouse model are monitored by PAM for 8 hours. The results show that PAM is able to noninvasively and continuously monitor the microcirculation and thus the severity of inflammatory response in LPS-injected mice.

2 | METHODS

2.1 | Experimental design

To investigate the changes in the microcirculation of the LPS-induced inflammation mouse model, 16 BALB/c male mice (Jiesijie, Shanghai, China) aged 10 to 12 weeks

(~25 g) were randomly divided into four groups (denoted as G1-G4) with four mice in each group. The four groups received LPS (L2630-100MG; Sigma-Aldrich, Saint Louis, Missouri) with concentrations of 0, 5, 15 and 30 mg/kg for G1-G4, respectively, where G1 was a control. As for validation of our LPS-induced inflammation mouse model, the detailed experimental methods and results can be found in Appendix S1. *In vivo* PAM images of mouse ear were taken right after the LPS was intraperitoneally injected at each mouse and every 1 hour during a period of 8 hours. For each PAM image, microvascular quantification (MQ) algorithm (details described later) was used to extract five vessel parameters for quantitative and statistical analysis.

2.2 | PAM system

The schematic of the PAM system is shown in Figure 1A. A 532 nm pulsed laser (FDSS532-Q3; CryLaS, Berlin, Germany) with <2 ns pulse duration and 1 kHz repetition rate was used for photoacoustic excitation. The laser was attenuated, spatially filtered and coupled into a double gradient-index lenses (DGLs) probe for laser focusing. The DGL probe enables high lateral resolution with long working distance. The details of the DGL probe can be found in our previous work [17]. The generated photoacoustic waves were detected by a custom-made needle hydrophone (central frequency: 35 MHz) placed obliquely with respect to the axial axis of the DGL probe, as shown in Figure 1B. The detected photoacoustic signals without averaging were amplified by a preamplifier (ZFL-500LN-BNC+; Mini-Circuits, Brooklyn, New York) and sampled by a high-speed digitizer (CSE1422, GaGe, Lockport, Illinois) with sampling rate of 200 MS/s and 14-bit resolution. The scan head consisting of the DGL probe and the hydrophone was mounted on a two-dimensional (2D) linear motorized stage (M-404; Physik Instrumente [PI], Karlsruhe, Germany) for scanning during image acquisition. The imaging system is capable of acquiring an image with 2 mm × 1 mm (500 × 250 scanning points with step size of 4 μm) within 5.8 minutes, which is mainly limited by the pulse repetition rate of the laser and the acceleration and deceleration time of the motorized stage. All PAM images were displayed in maximum amplitude projection (MAP) for further image processing and statistical analysis.

The anesthetized mouse (by injection of pentobarbital of 60 mg/kg) was fixed on a home-made animal platform. Before the experiment, the hair on the mouse ear was gently removed using a human-hair removing cream. During the experiment, the room temperature was kept around 26°C. The laser energy reaching the tissue surface was ~170 nJ/pulse. The measured half angle of the focused beam of the DGL probe was ~9.1°. By adjusting the optical focus at ~0.1 mm below the skin surface, the surface laser fluence can be estimated as 21 mJ/cm^2 [= (170 nJ)/(π × ((0.1 mm) × tan(9.1°))^2)], which was close to the American National Standards Institute safety limit (20 mJ/cm^2 for the visible
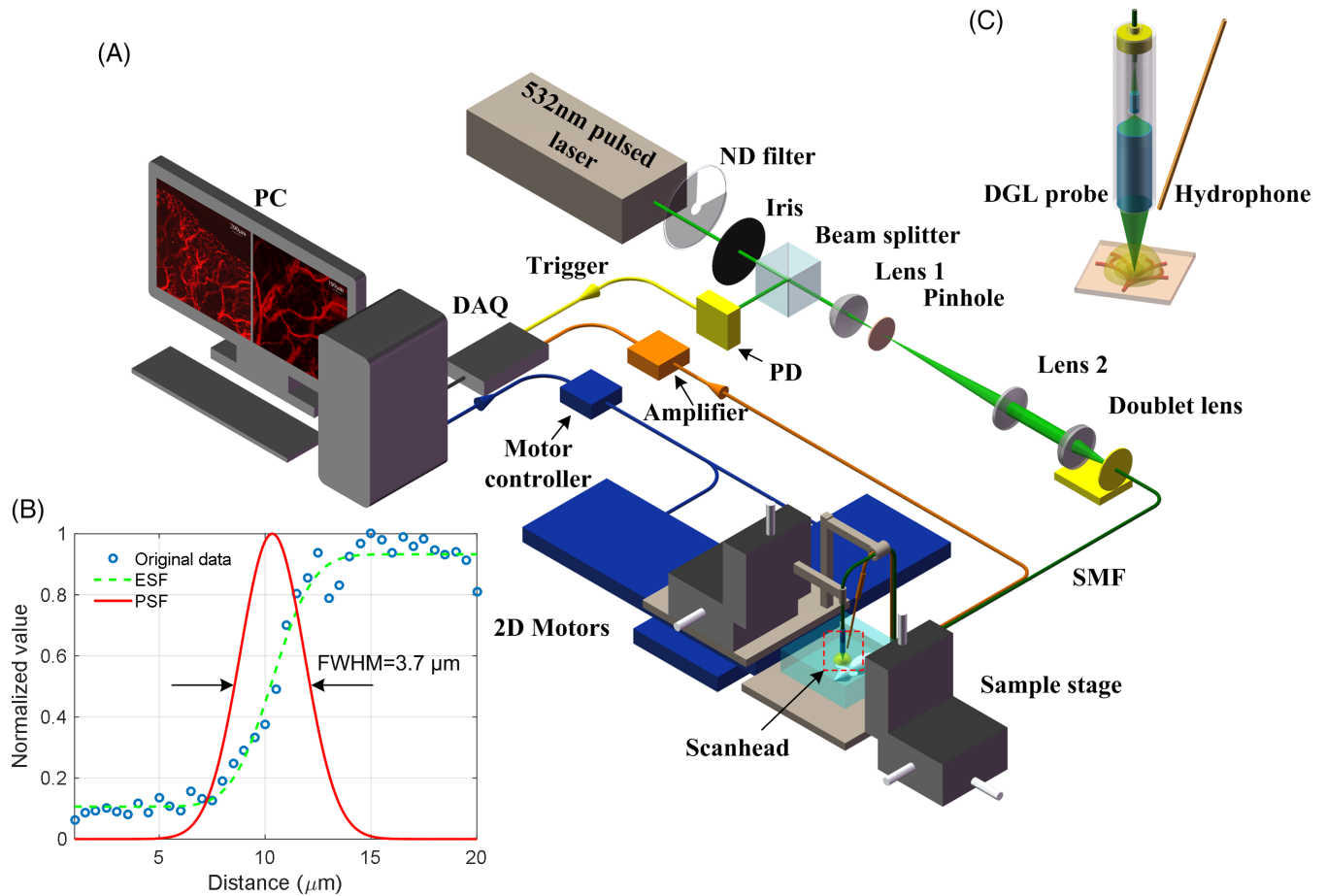
FIGURE 1 A, photoacoustic microscopy (PAM) system. B, schematic of scan head. C, calibration of lateral resolution. DAQ, data acquisition unit; ND, neutral density; PC, personal computer; PD, photodetector; SMF, single-mode fiber

wavelengths). All experimental animal procedures were carried out in conformity with the laboratory animal protocol approved by Laboratory Animal Care Committee of Shanghai Jiao Tong University.

To calibrate lateral resolution, the sharp edge of a razor blade was imaged with scanning step size of 0.5 μm. Figure 2C presents the original photoacoustic signal, and the one-dimensional profile was curve fitted by an edge spread function (ESF) [18]. Then, a line spread function (LSF) was calculated by taking the first derivative of the ESF. Finally, lateral resolution of 3.7 μm was determined by checking the full width at half maximum of the LSF. The theoretical resolution can be calculated by the expression: resolution = 0.51 × λ/(n × tanθ), where λ denotes the laser wavelength, n is the refractive index of the medium and θ is the half angle of the focused beam [17]. Thus, the theoretical resolution is ~1.3 μm [= 0.51 × (0.532 μm)/(1.33 × tan(9.1°)]. As a comparison, the measured value is much worse than the theoretical one, which is probably due to optical aberration of the gradient-index lenses [17].

2.3 | Image processing and statistical analysis

The overall flowchart of the MQ algorithm is shown in Figure 2A. First, we used Hessian matrix method to get the feature map of the blood vessels from the original PAM image [19]. The details of the feature map calculation can be found in Ref. [20]. Overall, the feature map presents better extraction of microvasculature, which will be illustrated by PAM images later. Second, the binarized image of blood vessels can be extracted from the feature map. Similarly, the details of the binarized image calculation can be found in Ref. [20]. Then, a Hilditch algorithm was used to identify the vascular centerlines from the binarized blood vessels [21]. Finally, as shown in Figure 2A, by using the original image, binarized image, and centerlines, the vessel parameters including (i) vessel density, (ii) vessel diameter, (iii) vessel ratio, (iv) vessel intensity, and (v) vessel tortuosity can be calculated, as detailed below.

(i) Vessel density: The vessel density is defined as the total length of the vessels over the observed area [22].

$$\text{Vessel density} = \frac{\text{Total vessel length}}{\text{Observed area}}. \tag{1}$$

Note that the total vessel length can be calculated from the vascular centerlines. Longer vessels in a region result in higher vessel density.

(ii) Vessel diameter: For each point on the centerline, according to its direction, the normal line (perpendicular to the direction of the centerline) can be calculated. Then, by
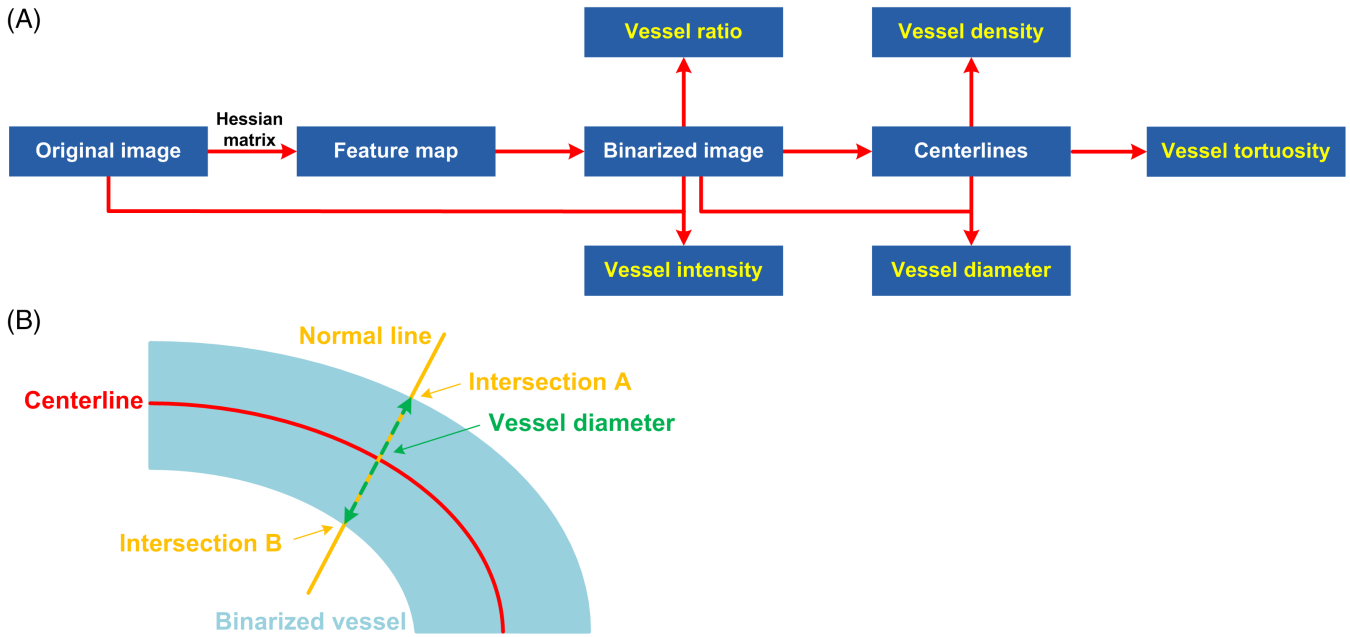
(A)

(B)

FIGURE 2   A, flowchart of the MQ algorithm. B, illustration of calculation of vessel diameter

comparing the normal line and the binarized vessel, Intersection A and Intersection B can be obtained, as illustrated in Figure 2B. The distance between the Intersection A and Intersection B is defined as the vessel diameter of each point along the centerline [20]. The average of the extracted vessel diameter at each point will be the final vessel diameter of the image.

(iii) Vessel ratio: The vessel ratio is defined as the proportion of the area of the blood vessels over the observed area.

$$\text{Vessel ratio} = \frac{\text{Vessel area}}{\text{Observed area}}. \quad (2)$$

Note that the vessel area can be calculated from the binarized image. From the above definitions of vessel parameters, vessel ratio is determined by both the vessel density (related to vessel length) and vessel diameter (related to vessel width).

(iv) Vessel intensity. Besides the shape of vessels, the changes in blood perfusion are also important. The vessel intensity is defined as the sum of the grayscale blood vessel map over the observed area. Note that the grayscale blood vessel map used here is the multiplication of the original image and the binarized image in order to exclude the possible background noise.

$$\text{Vessel intensity} = \frac{\sum(\text{Original image} \times \text{binarized image})}{\text{Observed area}}. \quad (3)$$

(v) Vessel tortuosity. The vessel tortuosity is also an important parameter for vascular disease assessment. In this study, the vessel tortuosity is defined as the ratio of the actual path length of a vessel to the linear distance between the two ends of that vessel [20, 23].

3 | RESULTS

To demonstrate the imaging capability of the PAM system and to illustrate the MQ algorithm described above, an area of 3 mm × 2.5 mm of the mouse ear was imaged with scanning step size of 4 μm (ie, 750 × 625 scanning points). The results are shown in Figure 3. The morphology of the microvasculature can be clearly observed in the 2D MAP image shown in Figure 3A. Figure 3B shows the depth-encoded MAP image over the scanning plane of Figure 3A, demonstrating the 3D imaging ability of the PAM system for this study. Figure 3C is the Hessian matrix feature map of Figure 3A. Compared with the original image (Figure 3A), the Hessian matrix algorithm can produce better results for vessel extraction, specifically better intensity uniformity for the extracted vessels in the feature map, as shown in the comparison of the images in the green dashed boxes in Figure 3A,C. Figure 3D shows the extracted blood vessels (i.e., binarized image) overlaid with the vessel centerlines by using the algorithm described above. It can be seen that, in general, the calculated centerlines (shown in red in Figure 3D) are accurately along the center of the extracted vessels (shown in blue in Figure 3D).

Furthermore, to validate the performance of the algorithm, the vasculature in three different regions (0.5 mm × 0.5 mm) in Figure 3A was quantified. The comparison of vessel density, vessel diameter, vessel ratio, vessel intensity and vessel tortuosity is shown in Table 1. It can be seen that the calculated vessel parameters agree well with visually observed characteristics. For example, Region [I] is close to the ear edge where capillaries are predominant. Because capillaries have many branches, Region (I) has the largest vessel density. The diameter of capillaries is only 6 to 8 μm, which leads to the smallest vessel diameter. Compared with Region
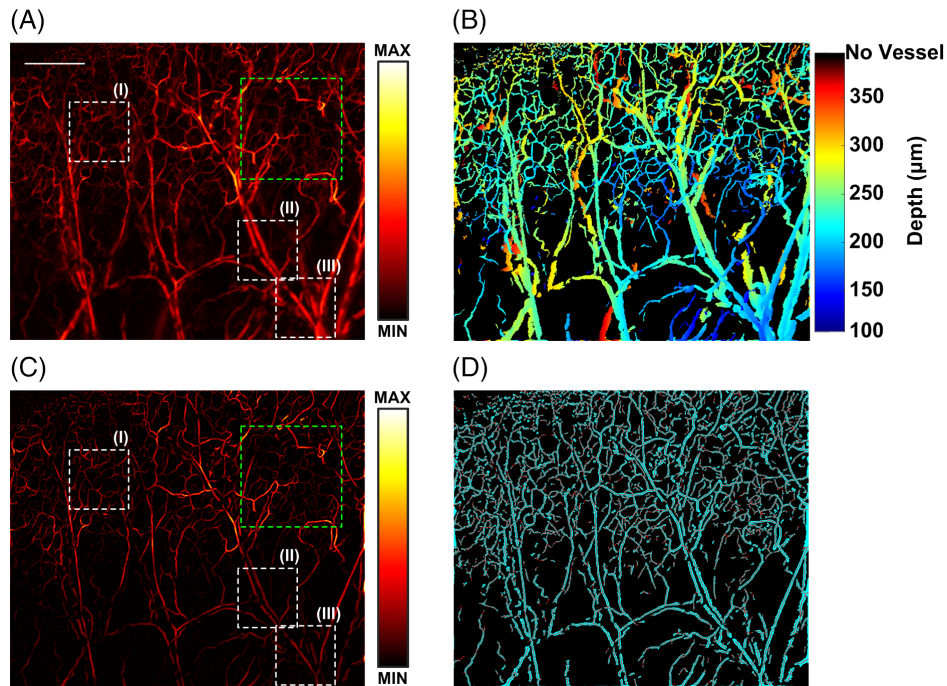
FIGURE 3 A, original image. Three regions (Region [I]-[III]) are chosen for comparing the vessel parameters. B, depth-encoded maximum amplitude projection (MAP) image. C, feature map. The same regions (white dashed boxes) corresponding to those in (A) are indicated for checking the change of the vessel diameter (discussed later). D, extracted blood vessels (ie, binarized image) overlaid with the vessel centerlines. The images in the green dashed boxes in (A) and (C) are to show better intensity uniformity in (C). All images share the same scale bar, which is 0.5 mm in length

TABLE 1 Comparison of vessel parameters among the three regions in Figure 3

Region	Vessel density	Vessel diameter (μm)	Vessel ratio	Vessel intensity	Vessel tortuosity
(I)	0.0897	8.2560	0.2780	0.0077	1.9332
(II)	0.0549	9.9718	0.2653	0.0104	1.2395
(III)	0.0472	11.1549	0.2847	0.0137	1.4259

(II) and Region [III], a similar vessel ratio in Region (I) results from the balanced effect of the largest vessel density (related to vessel length) and the smallest vessel diameter (related to vessel width). Besides, capillaries typically produce weaker photoacoustic signals compared with relatively large vessels, which results in the smallest vessel intensity considering similar vessel ratios in the three regions. Region (I) shows the largest vessel tortuosity because the small vessels and capillaries are typically more tortuous than large vessels. Region (III), on the contrary, has the smallest vessel density, the largest vessel diameter, and the largest vessel intensity, because in this region the majority is large vessels. Region (II) is similar to Region (III). Compared with Region (III), Region (II) has slightly larger vessel density, and slightly smaller vessel diameter and vessel intensity, which is also consistent with visualized characteristics. Although the vessel tortuosity of Region (II) is smaller than that of Region (III), the two values are close and are much smaller than that of Region (I), which is considered to be reasonable. The above results show that the PAM system can clearly image the mouse ear, and the MQ algorithm is able to properly provide vessel parameters by comparing them with visualized characteristics.

To study the quantitative changes of microvasculature and vessel parameters in the LPS-induced inflammation mouse model, the four groups of mice injected with different concentrations of LPS were imaged by PAM. As mentioned, four mice were used for each group in experiments, and PAM images were taken right after the injection of LPS and every 1 hour for 8 hours. All images were taken over an area of 2 mm × 1 mm on the mouse ear. For each mouse, images were taken from the same location during the observation period of 8 hours. Therefore, for each group, four sets of results (from four individual mice) can be used for statistical analysis. Figure 4 shows the representative PAM images from the G1 (0 mg/kg LPS as a control), G2 (5 mg/kg LPS), G3 (15 mg/kg LPS) and G4 (30 mg/kg LPS) at 0, 2, 4, 6 and 8 hours after the LPS injection. The corresponding vessel parameters are shown in Table 2.

As can be seen, first, for each group except G1, microvasculature decreases (ie, from plentiful to sparse blood vessels) over time. This can be better observed by checking the changes of vessels over time in the white dashed boxes (for G2-G4) in Figure 4. On the other hand, the microvasculature in G1 has been almost the same for 8 hours. Second, microvasculature decreases more rapidly for high-concentration
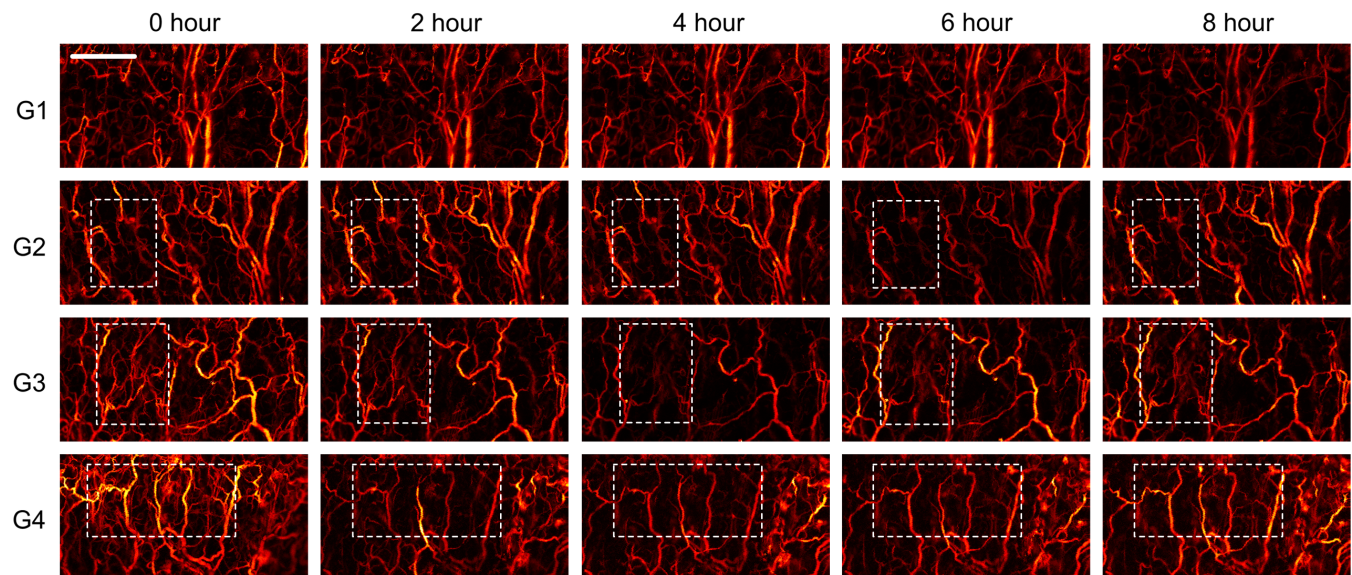
FIGURE 4 Representative photoacoustic microscopy (PAM) images of mouse ears. The images were taken 0 to 8 hours after the mice were treated with different concentrations of lipopolysaccharide (LPS). All images share the same scale bar, which is 0.5 mm in length. Each row corresponds to different concentrations of LPS (0, 5, 15, 30 mg/kg for G1-G4, respectively), and each column corresponds to different observation time (0, 2, 4, 6 and 8 hours after LPS administration)

TABLE 2 Normalized vessel parameters for different lipopolysaccharide (LPS) concentrations at different observation time (0, 2, 4, 6 and 8 h after LPS administration)

Vessel parameters	Group: LPS concentration (mg/kg)	0 h	2 h	4 h	6 h	8 h
Density	G1: 0	1.0000	0.9690	0.9239	0.9803	0.9141
	G2: 5	1.0000	0.9724	0.9855	0.9369	0.8213
	G3: 15	1.0000	0.8152	0.7890	0.7824	0.7484
	G4: 30	1.0000	0.7666	0.7488	0.7595	0.7133
Diameter	G1: 0	1.0000	0.9978	0.9776	0.9955	0.9826
	G2: 5	1.0000	1.0063	0.9874	1.0006	1.0377
	G3: 15	1.0000	1.0370	1.0578	1.0707	1.0366
	G4: 30	1.0000	1.0125	1.0217	0.9904	1.0190
Ratio	G1: 0	1.0000	0.9743	0.9499	0.9963	0.9463
	G2: 5	1.0000	0.9742	0.9812	0.9386	0.8847
	G3: 15	1.0000	0.8552	0.8418	0.8597	0.8386
	G4: 30	1.0000	0.8412	0.8356	0.8322	0.8037
Intensity	G1: 0	1.0000	1.017	0.9091	0.9318	0.8068
	G2: 5	1.0000	1.000	0.9000	0.9000	0.8000
	G3: 15	1.0000	0.5862	0.5103	0.5379	0.6069
	G4: 30	1.0000	0.3768	0.3043	0.3333	0.3043
Tortuosity	G1:0	1.0000	0.9455	0.9638	0.8914	0.9435
	G2: 5	1.0000	0.8938	1.0394	1.0852	1.1102
	G3: 15	1.0000	0.9524	0.9103	0.9895	0.9370
	G4: 30	1.0000	0.8090	0.8474	0.8430	0.8513

LPS than for low-concentration one. For example, by comparing the two images at 0 and 2 hours for G2-G4, it is observed that the two images at 0 and 2 hours for G2 are almost the same, while those for G4 are very different (ie, microvasculature decreases significantly.).

Figure 5 shows the statistical analysis of the changes of the five vessel parameters over time due to the administration of LPS with different concentrations. For each group, four sets of results (from four individual mice) were used to calculate the average values and SDs of vessel parameters. For each vessel parameter, by comparing the four curves corresponding to different LPS concentrations, a correlation between the vessel parameters and the applied LPS concentrations can be understood.
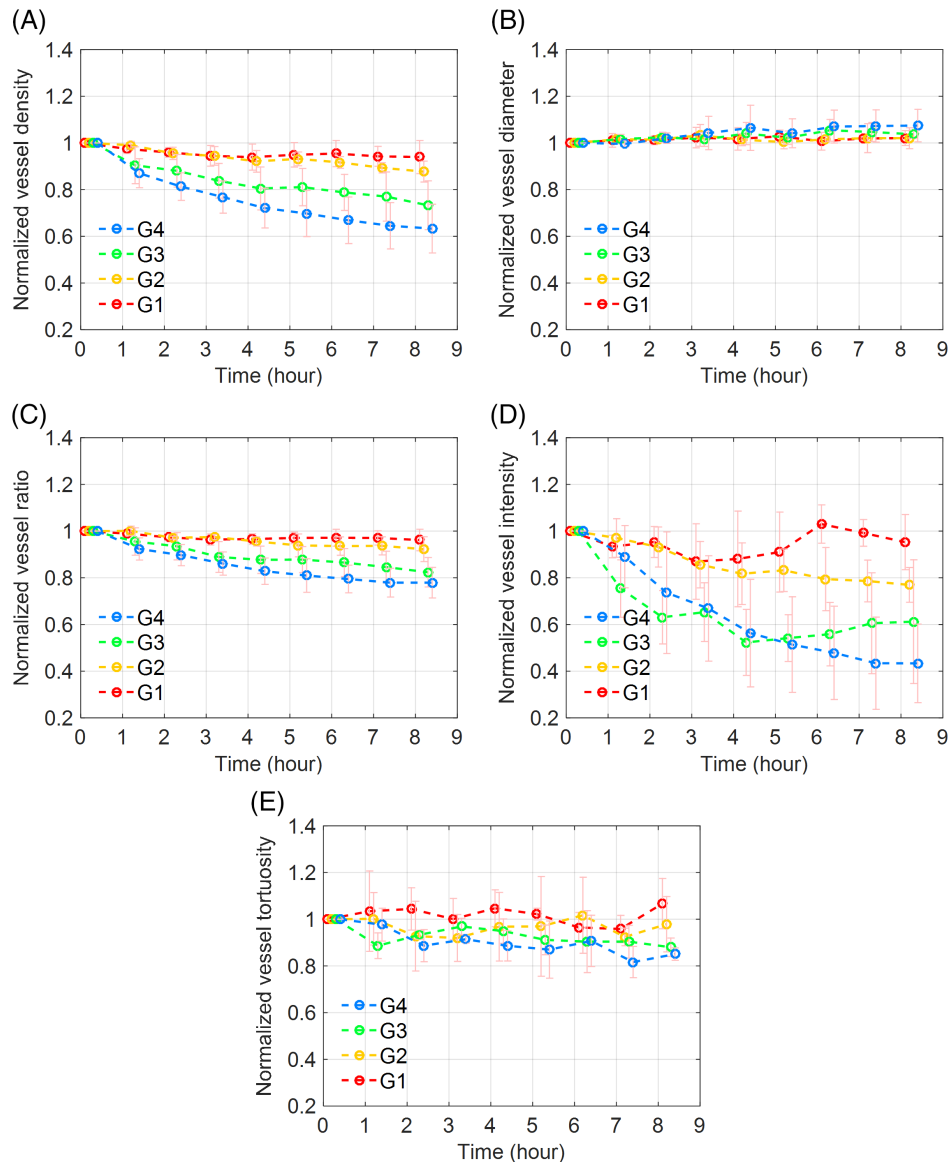
(A)

(B)

(C)

(D)

(E)

FIGURE 5 Statistical analysis of vessel parameters in mouse ear as time elapsed for different lipopolysaccharide (LPS) concentrations (ie, G1-G4). A, vessel density. B, vessel diameter. C, vessel ratio. D, vessel intensity. E, vessel tortuosity. All the curves are shifted a little along the x-axis to avoid the overlap of the error bars

Note that for better comparison, the curves were normalized to the average values at 0 hour, which better exhibits the relative changes over time for different concentrations. The normalization also mitigates the issue of sample differences among different groups. The STDs were scaled with the normalized average values. Relatively large STDs are observed in all the curves, which may be due to the following two reasons. First, there exist large sample-to-sample differences in different mice in each group. Second, there also exist large variations of microvasculature among different regions of the mouse ear for one individual mouse.

As can be seen in Figure 5, the vessel density, vessel ratio, vessel intensity and vessel tortuosity decrease as time elapsed for G2-G4. Besides, the higher the concentrations of the LPS, the more rapid the decreases of the four vessel parameters (ie, excluding vessel diameter)

over time for G2-G4. By comparing the parameters in the beginning and at the 8th hour, the changes of the four vessel parameters over the period of 8 hours are more drastic for high LPS concentrations than for low ones. Note that the four vessel parameters are kept almost the same over time for G1. On the other hand, the vessel diameter increases as time elapsed for G2-G4. This is because small vessels and capillaries disappeared while large vessels were retained, which leads to larger average vessel diameter. The rate of change of the vessel diameter vs LPS concentrations has a similar trend. The higher the concentrations of the LPS, the more rapid the increase of the vessel diameter over time for G2-G4. Besides, similarly, the changes of the vessel diameter over the period of 8 hours are more drastic for high LPS concentrations than for low ones, and the vessel diameter is kept almost the same over time for G1.

4 | DISCUSSION

In this work, we intend to verify that PAM may be a potential tool for monitoring microcirculation in sepsis. To mimic the pathology of sepsis (mainly *quantitative microcirculation disorder and organ dysfunction* caused by inflammatory response), the LPS-induced inflammation mouse model was employed (Appendix S1). LPS is the pathogenic component from the cell wall of gram-negative bacteria, which is the most common pathogenic microorganism causing sepsis. LPS administration can induce host inflammatory response, leading to the release of inflammatory mediators. Subsequently, it can cause damage of vascular endothelial cells and thus microcirculation disorder, eventually contributing to multiple organ dysfunction.

Recent studies suggest that the microcirculatory dysfunction plays a key role in the pathophysiologic process of sepsis. In the evaluation of sepsis, staged microcirculatory abnormalities in severity are closely associated with morbidity and mortality in septic patients [24]. Therefore, clinically applicable tools for accurate and effective evaluation of the modified microcirculation by various therapeutic approaches are critical to improving the treatment outcome of septic patients. PAM is able to monitor multi-parametric quantitative microcirculatory changes [16, 20]. In this aspect, the results shown in this work suggest that PAM holds promise to be a potential tool for early intervention of sepsis by identifying microcirculatory dysfunction in the early stages of inflammatory response, which may be helpful to avoid that some inflammatory response deteriorates into sepsis and even septic shock. Furthermore, PAM may provide guidance for treatment plan optimization of sepsis by being able to monitor the microcirculation changes during treatment of sepsis, which may facilitate immediate evaluation of the treatment effects and thus a timely adjustment of treatment plan.

Compared with sidestream dark-field imaging for monitoring the microcirculation changes, which is currently used in clinical practice, PAM has advantages in higher contrast, deeper penetration and being able to monitor functional information. PAM is also able to noninvasively and continuously monitor the microcirculation.

The present study demonstrated that PAM is a promising tool for studying microcirculatory alterations in sepsis. Unlike pure ultrasound imaging and OCT, PAM is speckle-free by taking advantage of the high optical absorption contrast of hemoglobin in red blood cells [25, 26], which is particularly useful in realizing quantitative measurement of changes in microvasculature in a more accurate way. High spatial resolution of PAM enables microcirculatory studies down to capillary level. The minimally invasive PAM technique enables longitudinal studies on the same location of the same animal sample, as demonstrated in this work. The 3D imaging ability may provide more comprehensive assessment.

As can be seen, from Figure 3A-C, the width of large vessels are reduced (eg, Region [III]) while that of small ones are kept the same (eg, Region [I]). This is due to the characteristic of the feature map calculation used in this work [19, 20]. The reduced width of large vessels in feature maps will lead to underestimation of the vessel diameter. To mitigate the issue, in this study (specifically, for Figures 4 and 5 and Table 2), we intentionally chose the image regions (2 mm × 1 mm) close to the ear edge, which consists of mainly small vessels.

In Figure 4, the photoacoustic signals of both small and large blood vessels are weakened at 2 hours compared to 0 hour. The phenomenon is more obvious for G3 and G4 (eg, high-concentration LPS). This might be due to the increase of capillary permeability, which promoted vascular leakage and the thickening of the tissue. As a consequence, the laser illumination was defocused. The exact reason is under investigation.

In this study, we investigated the morphological changes due to inflammatory response induced by LPS administration. As described previously, PAM offers unique capabilities in acquiring functional imaging such as sO_2 and blood flow. It is of medical significance to extend the current work to functional PAM for evaluating the LPS-induced inflammation mouse model. To acquire sO_2 by PAM, typically dual-wavelength photoacoustic excitation should be used [11, 14, 16]. Currently, our laser can only emit a single wavelength at 532 nm, which hinders the sO_2 measurement. We are upgrading our PAM system using a wavelength-tunable pulsed laser, which will enable the study of functional changes of sO_2 in the LPS-induced inflammation mouse model in our future work.

5 | CONCLUSION

In summary, PAM was used to evaluate the LPS-induced inflammation model in mice. Quantitative changes in microvasculature in response to various concentrations of LPS were examined and analyzed. We observed the decrease in microvasculature in a period of 8 hours after the LPS injection in mice. Besides, more drastic and faster decreases in microvasculature occurred for higher concentrations of LPS injection. The results show that PAM is able to noninvasively and continuously monitor the microcirculation and thus the severity of inflammatory response in LPS-injected mice. Furthermore, PAM holds promise to be a potential tool for early intervention of sepsis and may also provide guidance for treatment plan optimization of sepsis by investigating microcirculatory dysfunction.

AUTHOR BIOGRAPHIES

Please see Supporting Information online.

ORCID

Sung-Liang Chen https://orcid.org/0000-0002-0572-5110

REFERENCES

[1] M. Singer, C. S. Deutschman, C. W. Seymour, M. Shankar-Hari, D. Annane, M. Bauer, R. Bellomo, G. R. Bernard, J.-D. Chiche, C. M. Coopersmith, R. S. Hotchkiss, M. M. Levy, J. C. Marshall, G. S. Martin, S. M. Opal, G. D. Rubenfeld, T. van der Poll, J.-L. Vincent, D. C. Angus, *JAMA* **2016**, *215*, 801.

[2] H. B. Nguyen, E. P. Rivers, F. M. Abrahamian, G. J. Moran, E. Abraham, S. Trzeciak, D. T. Huang, T. Osborn, D. Stevens, D. A. Talan, *Ann. Emerg. Med.* **2006**, *48*, 28.

[3] H. Gomez, C. Ince, D. D. Backer, P. Pickkers, D. Payen, J. Hotchkiss, J. A. Kellum, *Shock* **2014**, *41*, 3.

[4] S. Eriksson, J. Nilsson, C. Sturesson, *Med. Devices (Auckl)* **2014**, *7*, 445.

[5] H. Cheng, Q. Luo, S. Zeng, S. Chen, J. Cen, H. Gong, *J. Biomed. Opt.* **2003**, *8*, 559.

[6] R. Bezemer, M. Legrand, E. Klijn, M. Heger, I. C. J. H. Post, T. M. van Gulik, D. Payen, C. Ince, *Opt. Express* **2010**, *18*, 15054.

[7] L. Themstrup, J. Welzel, S. Ciardo, R. Kaestle, M. Ulrich, J. Holmes, R. Whitehead, E. C. Sattler, N. Kindermann, G. Pellacani, G. B. E. Jemec, *Microvasc. Res.* **2016**, *107*, 97.

[8] J. Lee, Y. Gursoy-Ozdemir, B. Fu, D. A. Boas, T. Dalkara, *Appl. Optics* **2016**, *55*, 9526.

[9] L. V. Wang, S. Hu, *Science* **2012**, *335*, 1458.

[10] J. Yao, L. V. Wang, *Contrast Media Mol. Imaging* **2011**, *6*, 332.

[11] H. F. Zhang, K. Maslov, M. Sivaramakrishnan, G. Stoica, L. V. Wang, *Appl. Phys. Lett.* **2007**, *90*, 053901.

[12] S.-L. Chen, Z. Xie, P. L. Carson, X. Wang, L. J. Guo, *Opt. Lett.* **2011**, *36*, 4017.

[13] J. Yao, K. I. Maslov, Y. Zhang, Y. Xia, L. V. Wang, *J. Biomed. Opt.* **2011**, *16*, 076003.

[14] K. J. Rowland, J. Yao, L. Wang, C. R. Erwin, K. I. Maslov, L. V. Wang, B. W. Warner, *J. Pediatr. Surg.* **2012**, *47*, 1143.

[15] S.-L. Chen, J. Burnett, D. Sun, X. Wei, Z. Xie, X. Wang, *Biomed. Opt. Express* **2013**, *4*, 2657.

[16] B. Ning, M. J. Kennedy, A. J. Dixon, N. Sun, R. Cao, B. T. Soetikno, R. Chen, Q. Zhou, K. K. Shung, J. A. Hossack, S. Hu, *Opt. Lett.* **2015**, *40*, 910.

[17] Z. Guo, G. Li, S.-L. Chen, *J. Biophotonics* **2018**, *11*, e201800147.

[18] J. M. Boone, J. A. Seibert, *Med. Phys.* **1994**, *21*, 1541.

[19] A. F. Frangi, W. J. Niessen, K. L. Vincken, M. A. Viergever, *Med. Image Comput. Comput. Assist. Interv.* **1998**, *1496*, 130.

[20] Z. Yang, J. Chen, J. Yao, R. Lin, J. Meng, C. Liu, J. Yang, X. Li, L. Wang, L. Song, *Opt. Express* **2014**, *22*, 1500.

[21] M. Shimizu, H. Fukuda, G. Nakamura, 4th IEEE Southwest Symposium on Image Analysis and Interpretation, Austin, TX, USA, 2–4 **2000**.

[22] R. K. Jain, N. Safabakhsh, A. Sckell, Y. Chen, P. Jiang, L. Benjamin, F. Yuan, E. Keshet, *Proc. Natl. Acad. Sci. U. S. A.* **1998**, *95*, 10820.

[23] E. Bullitt, G. Gerig, S. M. Pizer, W. Lin, S. R. Aylward, *IEEE Trans. Med. Imaging* **2003**, *22*, 1163.

[24] G. Hernandez, A. Bruhn, C. Ince, *Curr. Vasc. Pharmacol.* **2013**, *11*, 161.

[25] Z. Guo, L. Li, L. V. Wang, *Med. Phys.* **2009**, *36*, 4084.

[26] J. Yao, L. V. Wang, *Laser Photonics Rev.* **2013**, *7*, 758.

SUPPORTING INFORMATION

Additional supporting information may be found online in the Supporting Information section at the end of the article.